Progress In Electromagnetics Research M, Vol. 99, 165–175, 2021

Bandpass Frequency Selective Surface Based on Square Waveguide Structure Using 3D Printing Technology

Zhengyong Yu[1] and Cheng Wang[2, *]

Abstract—In this paper, a novel three-dimensional (3D) bandpass frequency selective surface (FSS) is presented based on a square waveguide structure using 3D printing technology. The proposed 3D FSS is composed of a periodic array of the square waveguides with dumbbell slots embedded in waveguide walls. The square waveguide of the unit cell provides a propagation path, which can excite two resonant modes, leading to a bandpass response with one transmission pole and one transmission zero below the cutoff frequency of the square waveguide. To explain the operating principle of the proposed 3D FSS, the electric field distributions at the frequencies of transmission pole/zero are analyzed, and an equivalent circuit model is also established. For validation, a practical example is manufactured simply and rapidly, by using 3D printing technology. To verify the performance of the proposed 3D FSS, the frequency selective characteristics of the implemented 3D FSS for both TE and TM polarizations under different incident angles are measured. The measurement results show that the proposed structure exhibits dual polarizations and provides good frequency stability under incident angles from 0° to 40°.

1. INTRODUCTION

Frequency selective surfaces (FSSs), which can be regarded as generalized spatial filters, have been studied in the past few decades [1]. They have been widely used in antenna radomes [2], sub-reflectors [3], and electromagnetic shielding applications [4]. Traditional FSSs are based on an array of two-dimensional (2D) planar resonant elements, such as Jerusalem crosses, square or circular loops, square spirals, and plate types slots of various shapes [5, 6]. In general, these 2D FSS unit cells generate one resonant frequency, which fails to satisfy the performance requirements of practical applications. To achieve higher performance, various techniques have been proposed, such as multi-layered structures [7], fractal geometries [8], and multi resonant unit cells [9]. Recently, three-dimensional (3D) FSSs [10–22] become more and more attractive, because they can easily improve the filtering characteristics through an extra design degree of freedom, which are relatively difficult to realize by the conventional 2D FSSs.

The team of Prof. Shen firstly presented a novel 3D FSS in 2010, which consisted of a 2D periodic array of vertical microstrip lines [10]. Since the microstrip line supported two quasi-TEM modes in separated propagation paths, it was able to act as a dual-mode resonator, thus multiple transmission zeros/poles were produced to realize a pseudo-elliptic band-reject response. Based on this concept, various kinds of structures were presented to construct multimode resonators [11–17] for achieving desired frequency responses. By introducing shorting vias and rectangular metallic plates in two propagation paths, multiple transmission zeros were introduced to realize a wide out-of-band rejection [11]. The proposed FSS in [12], consisting of an array of three-layer printed circuit boards and a number of inserted metallic rods and printed patches, created two independent paths for providing a dual-band response. In [13], stacked parallel strip lines were employed for designing a 3D FSS,

Received 8 August 2020, Accepted 6 December 2020, Scheduled 10 December 2020

* Corresponding author: Cheng Wang (wangcheng0812@hotmail.com).

[1] School of Computer and Communication, Jiangsu Vocational College of Electronics and Information, Huai'an 223003, China.

[2] Shanghai United Imaging Healthcare Co., Ltd., Shanghai 201807, China.

resulting in triple stopbands. In addition, high frequency selectivity at both sides of the passband could be obtained by using multiple resonators with several horizontally placed metallic plates and vertically inserted metallic sheets [14]. Unfortunately, these 3D FSSs presented in [10–14] only operated under single polarization, which led to limitations on the practical applications. In order to achieve a dual-polarized response, a class of 3D FSSs was reported in [15–17]. These structures were still based on the 2D periodic array of vertical microstrip line resonators, whose unit cells were constructed by using a pair of double-sided parallel-strip lines [15], loop resonators [16], or stacked slotlines [17]. Furthermore, utilizing waveguides in 3D FSS could provide propagation paths to achieve multiple transmission zeros/poles for more interesting characteristics as well, such as sharp roll off [18], wide operating band [19], and mechanically tunability [20]. However, as reported in [10–20], most of the previous publications needed lots of building parts for assembly, hence the manufacturing process might be complex. Recently, as an advanced manufacturing technology, 3D printing is capable to rapidly fabricate objects from digital models. With the help of this new technology, the implementation of many complex structures in microwave applications, e.g., waveguide structures [21] and dielectric antennas [22], become easy and convenient.

In this paper, we present a new type of 3D FSS, which is constructed by an array of square waveguides with dumbbell slots embedded in waveguide walls. In the proposed 3D FSS, a dumbbell slot is equivalent to a resonator, which produces a slot resonance below the cutoff frequency of the square waveguide, leading to one transmission pole. Furthermore, a transmission zero is generated when the signals produced by the slot and square waveguide are out of phase in the waveguide propagation path. To explain the operating principle, an equivalent circuit model is established and investigated. By using 3D printing technology, a practical example is fabricated simply and rapidly. The results of measurement show good agreements with the simulated ones and verify that the response of the proposed 3D FSS is stable under oblique incidence for both TE and TM polarizations.

2. STRUCTURE AND OPERATING PRINCIPLE

2.1. Structure and Design Concept

As shown in Fig. 1(a), the proposed 3D FSS consists of a 2D periodic array of square waveguides. As indicated in Fig. 1(b), it is observed that the period of the unit cell along the x-axis or y-axis is p, with the thickness of the waveguide wall t. As a result, the internal side length of the waveguide is denoted as $w = p - 2t$. The height along z-axis of the waveguide is denoted by h. There is one dumbbell slot embedded in each surface of the square waveguide. In the dumbbell slot, the width and length of the central narrow slot are w_1 and l_1, respectively. At each end of the narrow slot, there is a wide slot, whose

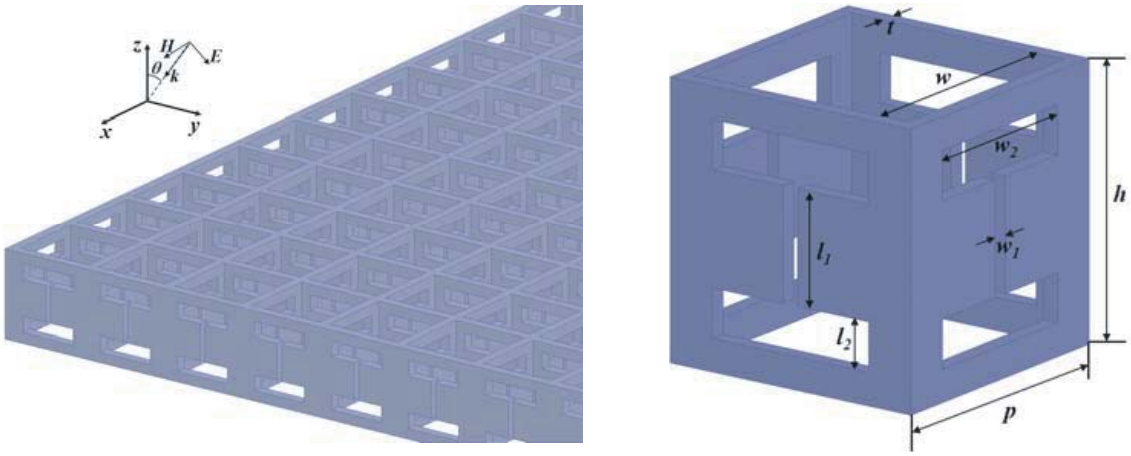

(a) (b)

Figure 1. The structure of the proposed 3D FSS. (a) Perspective view. (b) Geometry of the unit cell.

dimension is determined by w_2 and l_2. The proposed 3D FSS can realize dual polarizations naturally, because of the symmetrical geometry of the unit cells.

Firstly, an FSS based on a square waveguide structure without dumbbell slots is analyzed, as shown in Fig. 2. It is found that the square waveguide FSS has a highpass frequency response with the cutoff frequency about 10 GHz. Above the cutoff frequency, TE and TM modes can propagate. Moreover, below the cutoff frequency, only evanescent modes exist and cannot propagate. It is also observed that the Wood's anomalies [23] occur in the highpass band when the incident angle increases. This will deteriorate the flatness of the highpass band.

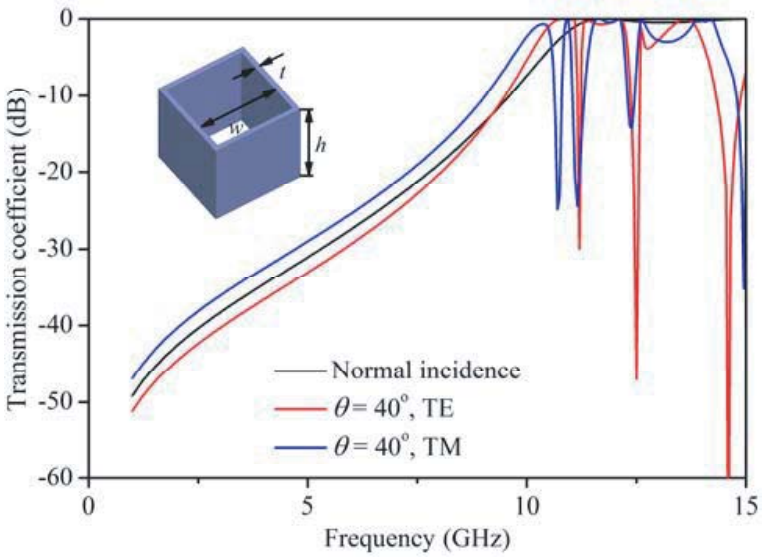

Figure 2. Simulated transmission coefficients of the square waveguide FSS at normal incidence and 40° incidence for both TE and TM polarizations ($w = 15$ mm, $h = 17$ mm, $t = 1$ mm).

From above analysis, the highpass band of the square waveguide FSS may not be suitable in the design of FSS. Therefore, the stopband produced by evanescent modes should be taken into account for generating a stable passband. Here, dumbbell slots are embedded in the square waveguide walls to construct the 3D FSS, by invoking the methodology of adding elements in the waveguide under evanescent mode for designing bandpass filters [24, 25]. The design parameters of the proposed 3D FSS with dumbbell slots are listed in Table 1. By using the full-wave software HFSS, the simulated transmission coefficients of the proposed 3D FSS at normal incidence are illustrated in Fig. 3. Comparing with the square waveguide FSS, it is observed that there is one transmission pole forming a passband centered at f_p (4.6 GHz). In addition, a transmission zero on the upper side of the passband is generated at f_z (7.8 GHz). In Fig. 3, f_c (11.7 GHz) and f_2 (12.6 GHz) are the cutoff frequencies of the square waveguide and the square waveguide with dumbbell slots, respectively. The obtained transmission pole and zero are located below the cutoff frequency of the square waveguide.

Table 1. Design parameters of the proposed 3D FSS.

Parameter	p	t	h	w_1	l_1	w_2	l_2
Value (mm)	17	1	17	1	7	11	3

Moreover, the angular sensitivity of the frequency response of the proposed 3D FSS for both TE and TM polarizations is also investigated by HFSS. Fig. 4 gives the transmission coefficients of the proposed 3D FSS at different incident angles (0°, 20°, and 40°) for both TE and TM polarizations. It is observed that the operating frequency (f_p) shifts about 2.3% at 40° incidence for TE polarization

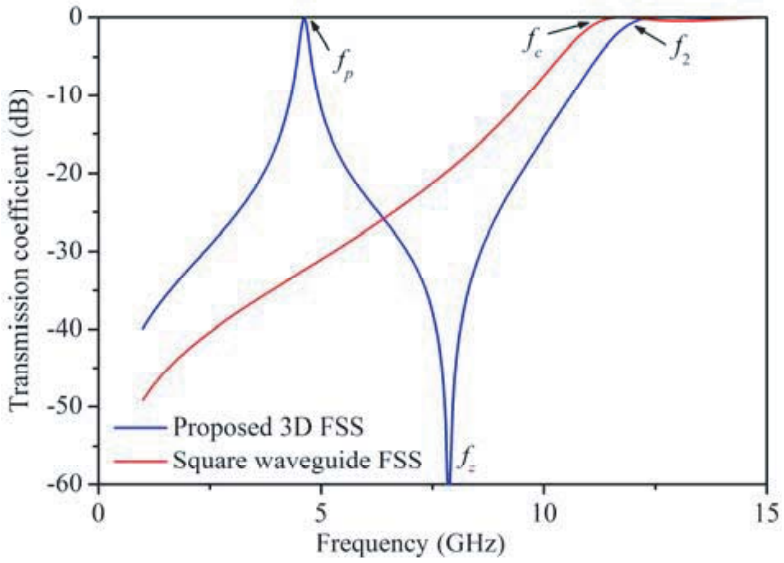

Figure 3. Simulated transmission coefficients of the square waveguide FSS and the proposed 3D FSS at normal incidence.

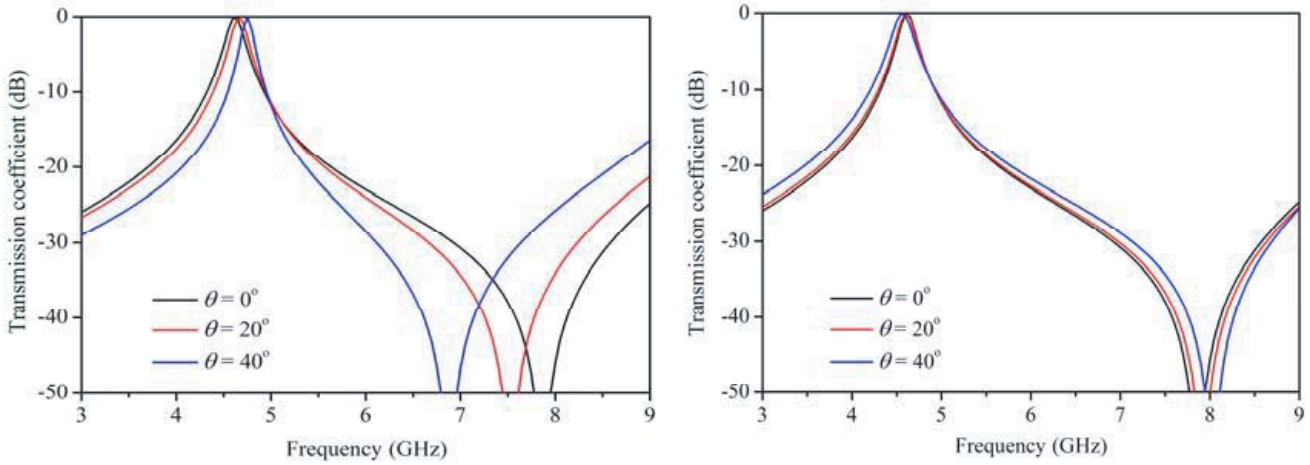

Figure 4. Simulated transmission coefficients of the proposed 3D FSS for different incident angles (0°, 20° and 40°). (a) TE polarization. (b) TM polarization.

and 0.8% at 40° incidence for TM polarization, which means that for oblique incident angles up to 40°, the frequency response of the proposed 3D FSS is relatively stable for both polarizations. For TE polarization, with the increase of incident angle, the magnetic-field along the z-axis direction excites another pair of slots along the y-axis direction, and the electrical length of the square waveguide with dumbbell slots is increased. Therefore, the transmission zero (f_z) shifts to the lower frequency. For TM polarization, another pair of slots are not excited, and the electrical length of the square waveguide with dumbbell slots is unchanged. Hence, the transmission zero keeps stable.

2.2. Operating Principle

In order to understand the operating principle, under TE polarization (E in the y-direction), the electric field distributions at the frequencies of f_p and f_z are shown in Fig. 5. It is found that two modes exist in

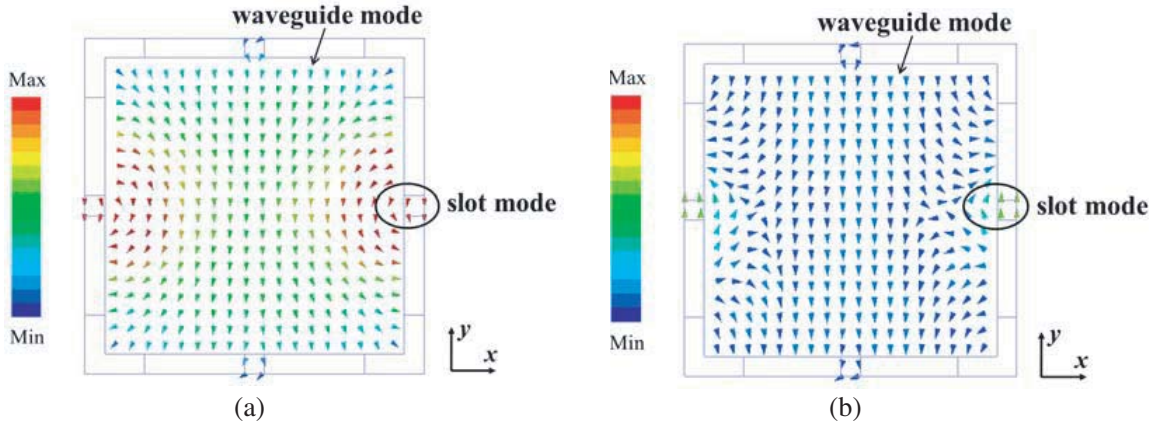

Figure 5. Electric field distributions of the proposed 3D FSS. (a) At transmission-pole frequency f_p. (b) At transmission-zero frequency f_z.

the square waveguide. One is supported by the dumbbell slots, namely, the slot mode. Then the second arises from the perturbed-waveguide mode, whose characteristic impedance and phase coefficient can be affected by the dumbbell slots. As seen in Fig. 5(a), the electric field at f_p is mainly produced by the resonance of the dumbbell slot, and the vectors of two modes are in phase, thus electromagnetic waves can propagate. Fig. 5(b) illustrates that the electric filed vectors of both modes are out of phase, leading to the transmission zero at f_z.

3. EQUIVALENT CIRCUIT MODEL

In this section, the equivalent circuit model is established to understand the operating principle, as illustrated in Fig. 6. The equivalent circuit model contains three cascaded sections. Part 1 and part 3 are both regular square waveguides with height h_1, which represents the waveguide structures without dumbbell slots. According to Fig. 7, for TE polarization (E in the y-direction), the electric field distribution at f_p is similar to that of evanescent TE_{10} mode of the square waveguide. As known in [15], there are two waveguide modes existing in the square waveguide. One mode is evanescent TE_{10} mode excited along the x-direction of the unit cell, and the other is evanescent TE_{01} mode excited along the y-direction of the unit cell. Since the E-field vectors of these two modes are very alike in distribution, thus the waveguide structure without slots is equivalent to two identical shunt transmission lines (Z_1, θ_1).

The frequency dependent characteristic impedance Z_1 and the electrical length θ_1 can be calculated as

$$Z_1 = \frac{\pi^2}{8} \frac{120\pi}{\sqrt{1-(f_c/f)^2}} \tag{1}$$

$$\theta_1 = h_1 \sqrt{(2\pi f)^2 \mu_0 \varepsilon_0 - (2\pi f_c)^2 \mu_0 \varepsilon_0} \tag{2}$$

where μ and ε represent the permeability and dielectric constant in free space, respectively.

In terms of part 2, it denotes the section of the square waveguide with dumbbell slots, with height h_2. For TE polarization (E in the y-direction), the periodic boundary condition is based on two PECs along the y-direction and two PMCs along the x-direction of the unit cell. In this condition, only the dumbbell slots along the x-direction are excited. Because part 2 is supported by a square waveguide with dumbbell slots, this part can be separated into two independent structures for analysis. Here, two series subnetworks $S1$ and $S2$ are used to model the waveguide and slots structure, respectively. Regarding $S1$, the waveguide modes are perturbed due to the existence of the slot modes. According to Eqs. (1) and (2), parameters f_c and h_1 are replaced by f_2 and h_2, respectively, and the frequency dependent characteristic impedance Z_2 and electrical length θ_2 are also obtained. As depicted in Fig. 8, the

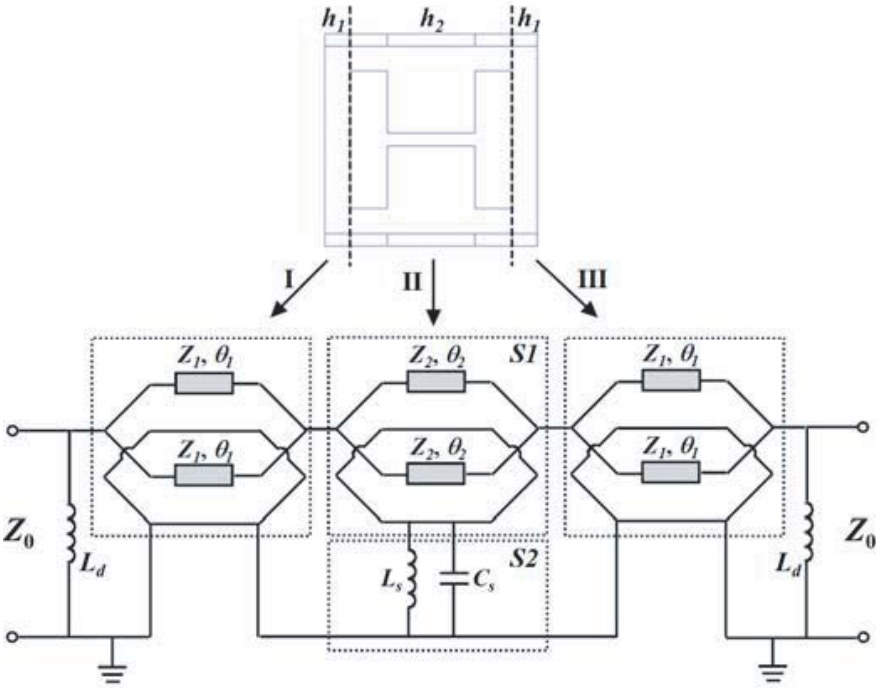

Figure 6. Equivalent circuit model of the proposed 3D FSS.

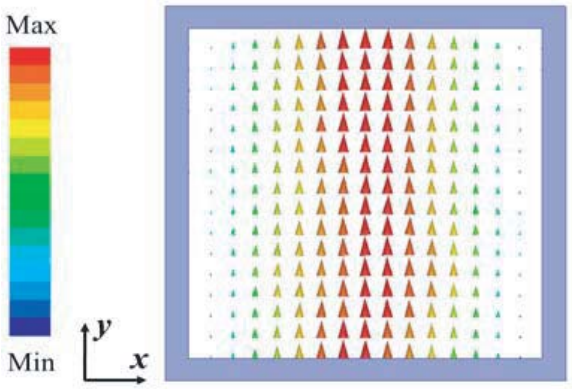

Figure 7. Electric field distribution at f_p in the square waveguide of part 1 and part 3.

electronic field is mainly concentrated in the narrow slot, while the current flows around the symmetric wide slots. Therefore, the subnetwork $S2$ of dumbbell slots can be represented by an LC resonator. Through the 3D quasi-static filed solver Q3D, the parameter values of the LC resonator can be extracted ($L_s = 2.08\,\text{nH}$, $C_s = 0.8\,\text{pF}$).

For accuracy, the discontinuities between the proposed structure and free space are considered in the equivalent circuit model. At the interface, a square loop can be used to express the discontinuity. According to the descriptions in [26], the square loop is represented by a frequency independent inductance L_d, and we can obtain its value using the following equation:

$$\frac{X_{L_d}}{Z_0} = \omega L_d = 2\cos\theta F\left(p, 2t, \lambda, \theta\right) \tag{3}$$

where θ is the incidence angle, and λ represents the operating wavelength of the square loop. The factor F representing normalized admittance is described in [27]. As a result, the discontinuity inductance L_d

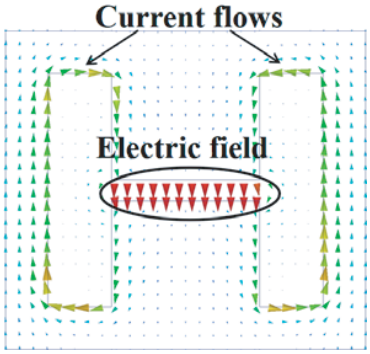

Figure 8. Sketch of the electric field and current flows for the dumbbell slot.

is 11.8 nH. With all these parameters, the transfer matrices of part 1 and part 3 can be written by

$$\begin{bmatrix} A_I & B_I \\ C_I & D_I \end{bmatrix} = \begin{bmatrix} \cos\theta_1 & jZ_1 \sin\theta_1/2 \\ 2j\sin\theta_1/Z_1 & \cos\theta_1 \end{bmatrix} \tag{4}$$

The transfer matrices of subnetworks $S1$ and $S2$ are expressed, respectively, as

$$\begin{bmatrix} A_{S1} & B_{S1} \\ C_{S1} & D_{S1} \end{bmatrix} = \begin{bmatrix} \cos\theta_2 & jZ_2 \sin\theta_2/2 \\ 2j\sin\theta_2/Z_2 & \cos\theta_2 \end{bmatrix} \tag{5}$$

$$\begin{bmatrix} A_{S2} & B_{S2} \\ C_{S2} & D_{S2} \end{bmatrix} = \begin{bmatrix} 1 & 0 \\ j\omega C_s + 1/(j\omega L_s) & 1 \end{bmatrix} \tag{6}$$

By connecting these two subnetworks in series, the impedance parameters of part 2 are given by

$$Z_{11} = Z_{22} = \frac{A_{S1}}{C_{S1}} + \frac{A_{S2}}{C_{S2}} \tag{7}$$

$$Z_{12} = Z_{21} = \frac{1}{C_{S1}} + \frac{1}{C_{S2}} \tag{8}$$

Then the transfer matrix of the equivalent circuit model is calculated as

$$\begin{bmatrix} A & B \\ C & D \end{bmatrix} = \begin{bmatrix} 1 & 0 \\ \dfrac{1}{j\omega L_s} & 1 \end{bmatrix} \begin{bmatrix} \cos\theta_1 & \dfrac{jZ_1\sin\theta_1}{2} \\ \dfrac{2j\sin\theta_1}{Z_1} & \cos\theta_1 \end{bmatrix} \times \begin{bmatrix} \dfrac{Z_{11}}{Z_{21}} & \dfrac{Z_{11}^2 - Z_{12}^2}{Z_{21}} \\ \dfrac{1}{Z_{21}} & \dfrac{Z_{22}}{Z_{21}} \end{bmatrix} \begin{bmatrix} \cos\theta_1 & \dfrac{jZ_1\sin\theta_1}{2} \\ \dfrac{2j\sin\theta_1}{Z_1} & \cos\theta_1 \end{bmatrix} \begin{bmatrix} 1 & 0 \\ \dfrac{1}{j\omega L_s} & 1 \end{bmatrix} \tag{9}$$

By using the conversion formula between S matrix and $ABCD$ matrix [28], S_{11} and S_{21} can be obtained as

$$S_{11} = \frac{A + B/Z_0 - CZ_0 - D}{A + B/Z_0 + CZ_0 + D} \tag{10}$$

$$S_{21} = \frac{2\,(AD - BC)}{A + B/Z_0 + CZ_0 + D} \tag{11}$$

where Z_0 is the characteristic impedance of the input and output ports, and the value is 377 Ω.

A comparison of the simulated transmission and reflection coefficients between the equivalent circuit model and HFSS is shown in Fig. 9. At frequency f_z, the discrepancy is mainly because the values of L_s and C_s are assumed to be quasi-static in the equivalent circuit model, while they are not accurate at high frequencies.

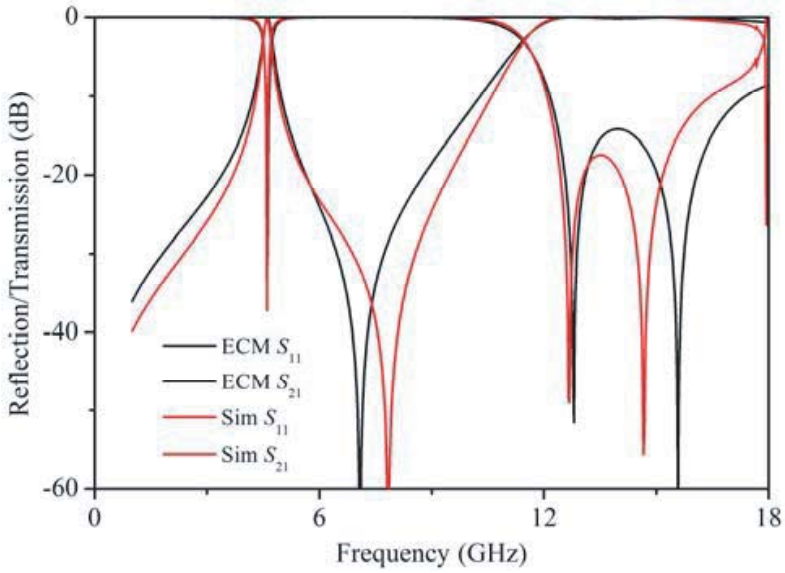

Figure 9. Reflection and Transmission coefficients of the proposed 3D FSS obtained by equivalent circuit model (ECM) and HFSS at normal incidence.

4. FABRICATION AND EXPERIMENT RESULTS

To validate the concept of the proposed 3D FSS, a practical example is fabricated. Because the proposed 3D FSS is an all-metal structure, it is possible to print the solid metal structure directly. Therefore, 3D printing technology is applied to realize easy and rapid prototyping in manufacture process. However with selective laser sintering (SLS), the cost is very expensive. Through A low-cost approach, the manufacture process contains two steps: 1) a framework of this structure is created by stereolithography apparatus (SLA) 3D printing with photosensitive resin material. With SLA 3D printing, a photosensitive resin is contained within a tank. The top of the tank is scanned with a UV laser, which selectively cures the top layer of resin. The 3D printed object sits on a platform within the tank. After one layer has been cured, the platform is lowered, and a fresh layer of resin is poured in front of the squeegee and leveled off by the squeegee. Then, the whole process is repeated. At last, the part is rinsed of excess resin and then fully cured in a UV oven. 2) After the frame was printed, a standard commercial electroless metal plating process is employed. Here, the frame is sequentially immersed in a series of chemical baths for surface preparation, surface activation, and metal deposition. With optimal conditions, this technique is able to uniformly coat the entire surface of the frame with a seed layer, which can then be electroplated with the desired metal material. Ultimately, a thin layer of metal is eventually plated on the surface of the frame. The metal material used for the conductive coating is an Ag-type paste with a viscosity of 14000 cps and an electrical resistance of $2.483 \times 10^{-5}\,\Omega \cdot \mathrm{cm}$. The thickness of the conductive coating is about $10\,\mu\mathrm{m}$, and the conductivity is approximately $4 \times 10^{6}\,\mathrm{S/m}$. As shown in Fig. 10, the manufactured prototype is approximately $27.2\,\mathrm{cm} \times 27.2\,\mathrm{cm}$ in size, which contains 16×16 (256) unit cells. The unit cell size is $0.26\lambda_0 \times 0.26\lambda_0 \times 0.26\lambda_0$, where λ_0 is the wavelength in free space at the center frequency.

The manufactured prototype is measured by free-space method. A photograph of the measurement setup is shown in Fig. 11. There are two wideband horn antennas (operating from 1 to 18 GHz), the FSS prototype, the rotatable screen covered by absorbers, and a vector network analyzer. The FSS prototype is placed within the rectangular through-hole window in the center of the rotatable screen for the measurement of incident stability. A pair of horn antennas are located about 160 cm apart from each side of the centered rotatable screen to satisfy the far-field condition, so that a uniform plane wave strike upon the FSS. The two horn antennas are connected by the vector network analyzer. Moreover, the measurement device is surrounded by using absorbing screens, so the contribution of

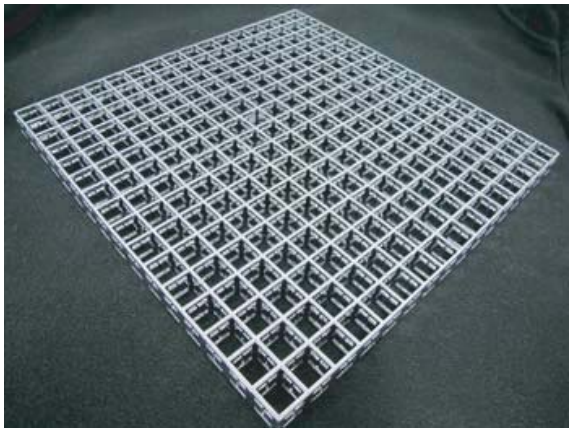

Figure 10. Photograph of the fabricated 3D FSS.

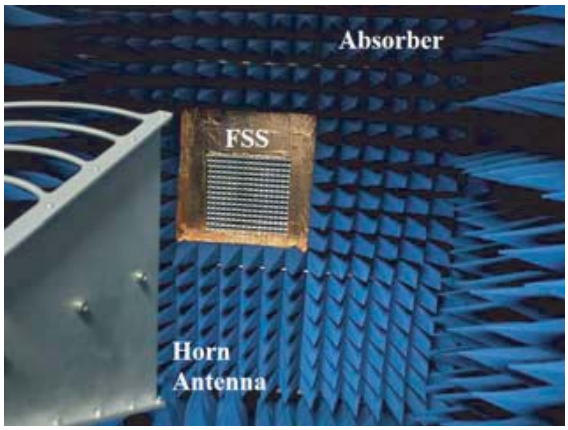

Figure 11. Photograph of the measurement setup.

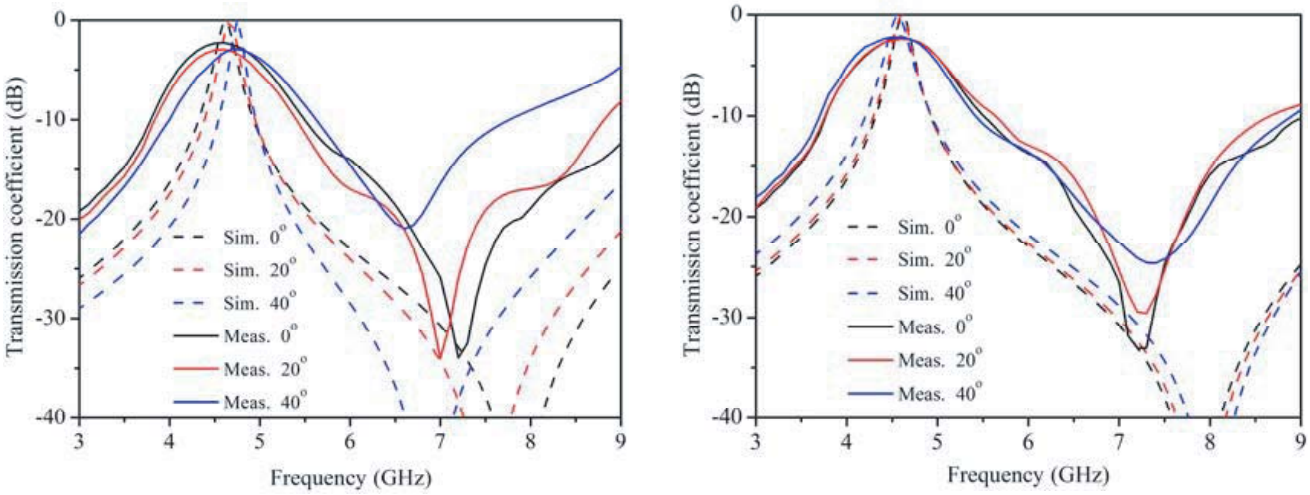

Figure 12. Measured transmission coefficients of the proposed 3D FSS for different incident angles. (a) TE polarization. (b) TM polarization.

diffraction can be negligible. For obtaining the measured transmission coefficients, the propagation loss is firstly eliminated by the normalization of the measured results without the FSS prototype, and the environment noise is eliminated by the measured results of an identically-sized metallic plate. Moreover, the time-domain gating function of the vector network analyzer is applied to calibrate the measured results for considering the multipath effects.

Figure 12 shows the measured frequency response of the prototype under different incident angles (0°, 20°, and 40°) for both TE and TM polarizations. From the measured results, it is observed that the proposed 3D FSS realizes a passband around 4.6 GHz and a transmission zero operates at about 7.3 GHz under normal incidence. Moreover, the prototype provides a stable angular response from 0° to 40° for both polarizations. Compared with simulated results, the measured 3 dB bandwidths of the passband are widened due to the decrease of the Q-factor for the fabricated 3D FSS. There is frequency offset of the transmission zero, which is mainly caused by relatively low resolution of SLA 3D printing. Moreover, the measured insertion loss of the passband (2.1 dB) is larger than the simulated one (0.6 dB) under normal incidence, which results from poor electrical conductivity of the plated metal and the conductor losses unconsidered in the simulated model. The other acceptable discrepancies between the

simulated and measured results may also be attributed to fabrication tolerances and measurement error. However, the measured results can prove the feasibility of the proposed 3D FSS.

5. CONCLUSION

In this paper, a dual-polarized bandpass 3D FSS based on a square waveguide structure has been presented, which operates below the cutoff frequency of the square waveguide. The proposed structure is capable to generate one transmission pole for a passband by the dumbbell slots embedded in square waveguide walls. In addition, one transmission zero is introduced when the electric field vectors are out of phase in the slots and waveguides. An equivalent circuit model is presented for better understanding the operating principle. A prototype is fabricated quickly and easily by using 3D printing technology. The measured results of the fabricated prototype show a comparable agreement with the simulated results, which can verify the feasibility of the proposed 3D FSS. Based on this design concept, various shapes of slots may be introduced to obtain more 3D FSSs with attractive filtering responses by multiple transmission poles/zeros in the future.

ACKNOWLEDGMENT

This work was supported by Doctor Studio Project Qing Lan Project Natural Science Foundation of the Jiangsu Higher Education Institutions of China (No. 19KJB510002), "333 Project" Research Funding Project of Jiangsu Province (No. BRA2018315), National Natural Science Foundation of China (No. 61571232), and Huai'an Innovation Service Capacity Construction Project (HAP201904).

REFERENCES

1. Munk, B. A., *Frequency Selective Surface: Theory and Design*, Wiley, New York, NY, USA, 2000.
2. Chen, H., X. Hou, and L. Deng, "Design of frequency selective surfaces radome for a planar slotted waveguide antenna," *IEEE Antennas Wireless Propag. Lett.*, Vol. 8, 1231–1233, 2009.
3. Song, X., Z. Yan, T. Zhang, C. Yang, and R. Lian, "Triband frequency selective surface as subreflector in Ku-, K-, and Ka-bands," *IEEE Antennas Wireless Propag. Lett.*, Vol. 15, 1869–1872, 2016.
4. Sivasamy, R., M. Kanagasabai, S. Baisakhiya, R. Natarajan, J. K. Pakkathillam, and S. K. Palaniswamy, "A novel shield for GSM 1800 MHz band using frequency selective surface," *Progress In Electromagnetics Research Letters*, Vol. 38, 193–199, 2013.
5. Zhang, K. Z., W. Jiang, J. Y. Ren, and S. X. Gong, "An annular-ring miniaturized stopband frequency selective surface with ultra-large angle of incidence," *Progress In Electromagnetics Research M*, Vol. 65, 19–27, 2018.
6. Wu, R., H. Zhang, Z. M. Yang, T. Zhong, and Y. F. Lin, "Compact stable frequency selective surface using novel Y-type element," *Progress In Electromagnetics Research Letters*, Vol. 57, 85–90, 2015.
7. Shaik, V. and K. Shambavi, "Design of dodecagon unit cell shape based three layered frequency selective surfaces for X band reflection," *Progress In Electromagnetics Research M*, Vol. 75, 103–111, 2018.
8. Xue, J. Y., S. X. Gong, P. F. Zhang, W. Wang, and F. F. Zhang, "A new miniaturized fractal frequency selective surface with excellent angular stability," *Progress In Electromagnetics Research Letters*, Vol. 13, 131–138, 2010.
9. Wang, H., M. Yan, S. Qu, L. Zheng, and J. Wang, "Design of a self-complementary frequency selective surface with multi-band polarization separation characteristic," *IEEE Access*, Vol. 7, 36788–36799, 2019.
10. Rashid, A. K. and Z. Shen, "A novel band-reject frequency selective surface with pseudo-elliptic response," *IEEE Trans. Antennas Propag.*, Vol. 58, No. 4, 1220–1226, 2010.
11. Li, B. and Z. Shen, "Three-dimensional bandpass frequency-selective structures with multiple transmission zeros," *IEEE Trans. Microw. Theory Techn.*, Vol. 61, No. 10, 3578–3589, 2013.

12. Li, B. and Z. Shen, "Dual-band bandpass frequency-selective structures with arbitrary band ratios," *IEEE Trans. Antennas Propag.*, Vol. 62, No. 11, 5504–5512, 2014.
13. Al-Sheikh, A. and Z. Shen, "Design of wideband bandstop frequency selective structures using stacked parallel strip line arrays," *IEEE Trans. Antennas Propag.*, Vol. 64, No. 8, 3401–3409, 2016.
14. Tao, K., B. Li, Y. Tang, M. Zhang, and Y. Bo, "Analysis and implementation of 3D bandpass frequency selective structure with high frequency selectivity," *Electron. Lett.*, Vol. 53, No. 22, 324–326, 2017.
15. Omar, A. A. and Z. Shen, "Double-sided parallel-strip line resonator for dual-polarized 3-D frequency-selective structure and absorber," *IEEE Trans. Microw. Theory Techn.*, Vol. 65, No. 10, 3744–3752, 2017.
16. Omar, A. A. and Z. Shen, "Thin bandstop frequency-selective structures based on loop resonator," *IEEE Trans. Microw. Theory Techn.*, Vol. 65, No. 7, 2298–2309, 2017.
17. Li, B., X. Huang, L. Zhu, Y. X. Zhang, Y. M. Tang, W. J. Lu, and Y. M. Bo, "Bandpass frequency selective structure with improved out-of-band rejection using stacked single-layer slotlines," *IEEE Trans. Antennas Propag.*, Vol. 66, No. 11, 6003–6014, 2018.
18. Rashid, A. K., Z. Shen, and B. Li, "An elliptical bandpass frequency selective structure based on microstrip lines," *IEEE Trans. Antennas Propag.*, Vol. 60, No. 10, 4661–4669, 2012.
19. Pelletti, C., G. Bianconi, R. Mittra, and Z. Shen, "Frequency selective surface with wideband quasi-elliptic bandpass response," *Electron. Lett.*, Vol. 49, No. 17, 1052–1053, 2013.
20. Ferreira, D., I. Cuiñas, R. F. S. Caldeirinha, and T. R. Fernandes, "3-D mechanically tunable square slot FSS," *IEEE Trans. Antennas Propag.*, Vol. 65, No. 1, 242–250, 2017.
21. Zhang, B. and H. Zirath, "Metallic 3-D printed rectangular waveguides for millimeter-wave applications," *IEEE Trans. Compon. Packag. Manuf. Technol.*, Vol. 6, No. 5, 796–804, 2016.
22. Nayeri, P., et al., "3D printed dielectric reflectarrays: Low-cost high-gain antennas at sub-millimeter waves," *IEEE Trans. Antennas Propag.*, Vol. 62, No. 4, 2000–2008, 2014.
23. Wu, T. K. (ed.), *Frequency Selective Surface and Grid Array*, Wiley, New York, NY, USA, 1995.
24. Craven, G. F. and C. K. Mok, "The design of evanescent mode waveguide bandpass filters for a prescribed insertion loss characteristic," *IEEE Trans. Microw. Theory Tech.*, Vol. 19, No. 3, 295–308, 1971.
25. Dong, Y. D., T. Yang, and T. Itoh, "Substrate integrated waveguide loaded by complementary split-ring resonators and its applications to miniaturized waveguide filters," *IEEE Trans. Microw. Theory Tech.*, Vol. 57, No. 9, 2211–2223, 2009.
26. Sarabandi, K. and N. Behdad, "A frequency selective surface with miniaturized elements," *IEEE Trans. Antennas Propag.*, Vol. 55, No. 5, 1239–1245, 2007.
27. Lee, C. K. and R. J. Langley, "Equivalent-circuit models for frequency selective surfaces at oblique angles of incidence," *IEE Proc. H — Microw., Antennas Propag.*, Vol. 132, No. 6, 395–399, 1985.
28. Pozar, D. M., *Microwave Engineering*, Wiley, Hoboken, NJ, USA, 2009.